ADVANCED MATERIALS TECHNOLOGIES
www.advmattechnol.de

Multimaterial Multinozzle Adaptive 3D Printing of Soft Materials

*Sebastien G. M. Uzel, Robert D. Weeks, Michael Eriksson, Dimitri Kokkinis, and Jennifer A. Lewis**

Direct ink writing is a facile method that enables biological, structural, and functional materials to be printed in three dimensions (3D). To date, this extrusion-based method has primarily been used to soft materials in a layer-wise manner on planar substrates. However, many emerging applications would benefit from the ability to conformally print materials of varying composition on substrates with arbitrary topography. Here, a high throughput platform based on multimaterial multinozzle adaptive 3D printing (MMA-3DP) that provides independent control of nozzle height and seamless switching between inks is reported. To demonstrate the MMA-3DP platform, conformally pattern viscoelastic inks composed of triblock copolymer, gelatin, and photopolymerizable polyacrylate materials onto complex substrates of varying topography, including those with surface defects that mimic skin abrasions or deep gouges. This platform opens new avenues for rapidly patterning soft materials for structural, functional, and biomedical applications.

1. Introduction

Direct ink writing (DIW) is an extrusion-based 3D printing method that enables patterning of a broad array of functional,[1–6] structural,[7–12] and biological[13–21] materials in three dimensions. To date, this method has been primarily limited to the layer-wise deposition of viscoelastic inks through a single nozzle onto planar substrates. Yet the ability to rapidly pattern multiple materials simultaneously onto substrates with arbitrary topography would be advantageous for many applications including structural defect repair, and wound repair, and tissue regeneration. New printhead designs are needed to unleash the full potential of high-throughput, conformal 3D printing of multiple materials. Important steps toward this goal have recently emerged, including printheads capable of seamlessly switching between two or more viscoelastic inks through single[22] or multiple nozzles[23] on planar surfaces as well as adaptive printheads capable of patterning a single viscoelastic ink through one nozzle on nonplanar substrates.[24–26] However, the integration of conformal 3D printing with multimaterial multinozzle printheads has yet to be realized.

Here, we report a multimaterial, multinozzle adaptive 3D printing (MMA-3DP) method for conformally patterning soft matter onto arbitrary substrates. We first designed, fabricated, and characterized these MMA-3D printheads to ensure that high fidelity patterns could be printed onto nonplanar substrates with high throughput. To assess their performance, we used a viscoelastic ink composed of an aqueous-based triblock copolymer gel. Next, we integrated solenoid valves within the MMA-3D printheads to control ink flow (on/off switching) through the nozzles during printing. Finally, we used this new platform to rapidly repair or infill complex 3D objects, including a simple wound (abrasion) model generated on a mannequin forearm using a gelatin-based (hydrogel) ink and a deep surface gouge created in a periodic architecture composed of alternating stiff and soft layers using two polyacrylate inks.

2. Results and Discussion

The design and implementation of our MMA-3DP method is highlighted in **Figure 1**. Our method involves four steps (Figure 1A): first, a line profilometer scans a region of interest and collects arrays of 800 data points at regular intervals in the *y*-direction (direction of printing). Next, the substrate topography is extrapolated from the resulting point cloud, then individual print paths are computed for each nozzle of the printhead array. Finally, these trajectories are used to guide the printhead, which can conformally pattern ink filaments over complex substrate topography. The multinozzle printhead contains 16 nozzles, spaced 2.5 mm apart, and positioned in an interdigitated fashion (Figure 1B, Figure S1A,B, Supporting Information). The two sets of eight nozzles are supplied by ink reservoirs through 3D printed manifolds that are connected to flexible tubing to accommodate nozzle displacement in the *z*-direction (Figure 1B and Figure S1C, Supporting Information). Note, viscous losses that arise due to this lengthy tubing coupled with the maximum pressure sustainable by the barbed fittings

S. G. M. Uzel, J. A. Lewis
Wyss Institute for Biologically Inspired Engineering
Harvard University
Cambridge, MA 02138, USA
E-mail: jalewis@seas.harvard.edu

S. G. M. Uzel, R. D. Weeks, M. Eriksson, D. Kokkinis, J. A. Lewis
John A. Paulson School of Engineering and Applied Sciences
Harvard University
Cambridge, MA 02138, USA

The ORCID identification number(s) for the author(s) of this article can be found under https://doi.org/10.1002/admt.202101710.

DOI: 10.1002/admt.202101710

 © 2022 Wiley-VCH GmbH

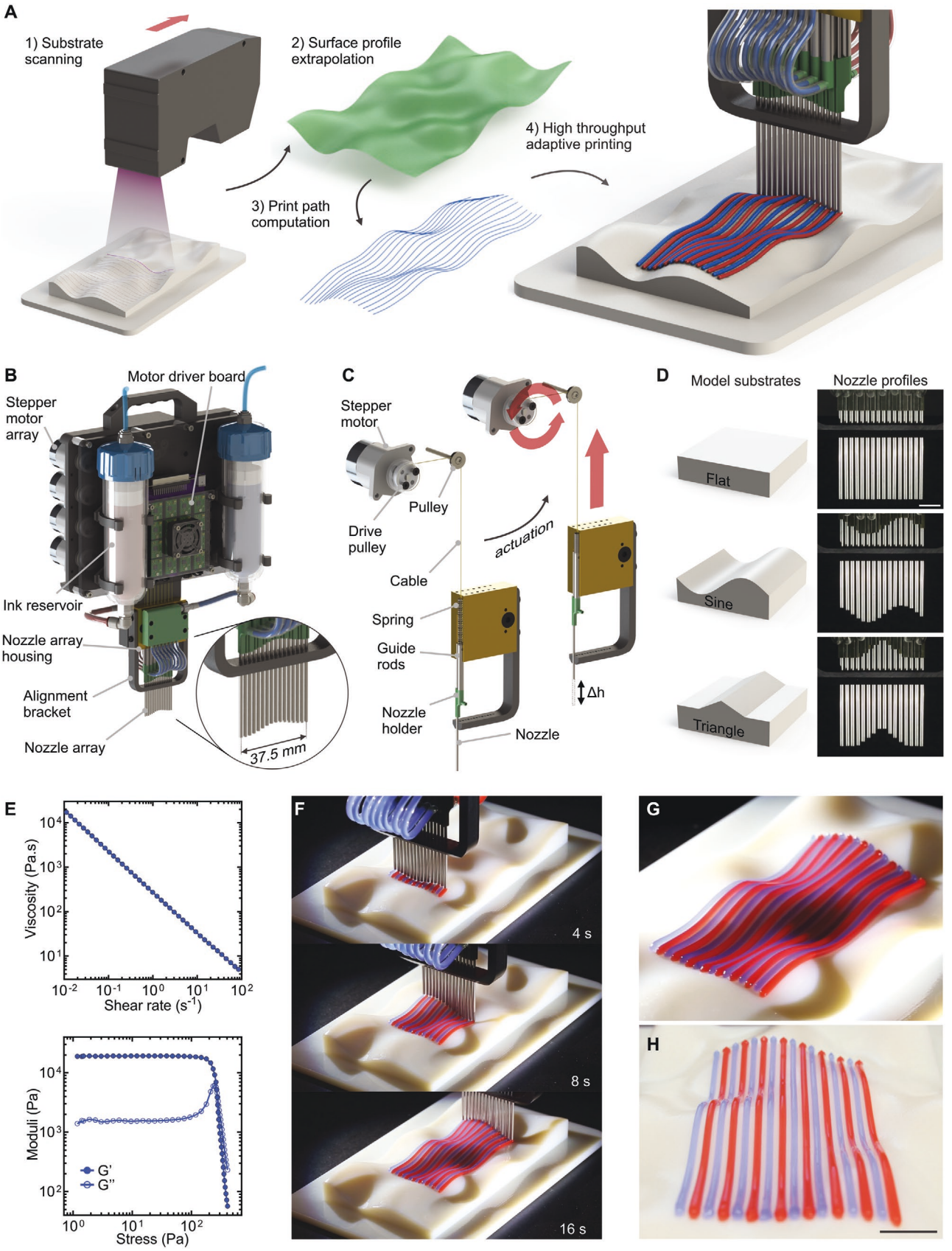

© 2022 Wiley-VCH GmbH

(≈80 PSI or 550 kPa) limit the maximum ink viscosity that can be extruded to roughly two-fold higher than those used here. Each spring-loaded nozzle is connected to a geared stepper motor, converting the rotatory motion into a linear displacement of the nozzle along the z-direction with a total amplitude Δh of 25 mm (Figure 1C). This design was inspired by the placement of tendons in the carpal tunnel, which transmit force from the forearm muscles to the multiple phalanges. Specifically, by moving the actuators away from the printhead, a compact arrangement of multiple nozzles within the MMA printheads is achieved. This method of actuation results in minimal backlash and stiction (Figure S2A, Supporting Information), yielding an average position error of 34 µm over a 10-mm range of motion and across all 16 nozzles (Figure S2B, Supporting Information), with a repeatability of 2.4 (±11.1) µm over a series of 100 command requests per nozzle (1600 requests in total) (Figure S2C, Supporting Information). The dynamic and coordinated motion of this multinozzle array enables the MMA printhead to adopt complex configurations that conform to the topography of the underlying surface, as illustrated on virtual substrates with flat, sinusoidal, or triangular geometries (Figure 1D, Movie S1, Supporting Information). Using this technique, we adaptively printed a model viscoelastic ink composed of an aqueous-based triblock copolymer gel onto a 3D printed substrate with a randomly generated topography. Note, different pigments (red and blue) are added to this ink solely to aid visualization. The observed shear-thinning behavior gives rise to an apparent viscosity of ≈3–5 Pa s at relevant shear rates 10–50 s^{-1} facilitating its flow during printing, while its plateau storage modulus of ≈20 kPa allows the patterned ink filaments to maintain their cylindrical shape upon exiting each nozzle (Figure 1E). We co-print multiple ink filaments using this adaptive nozzle array, in which each nozzle independently conforms to the substrate topography by moving their height up and down in the z-direction, as the MMA printhead is translated in the y-direction at a speed of 5 mm s^{-1} (Figure 1F, Movie S2, Supporting Information) resulting in high pattern fidelity (Figure 1G,H). By contrast, the pattern fidelity is drastically reduced when the same MMA printhead is used to deposit ink filaments through nozzles held at a fixed height (Figure S3, Supporting Information), akin to standard (nonconformal) DIW.

Next, we quantified the effects of different printing modes on pattern fidelity by altering the printing parameters and nozzle design. For example, discrete ink filaments are produced during MMA-3DP using an optimal pressure of ≈275 kPa and maintaining each nozzle at a height of 1.8 mm as the MMA printhead is translated across a substrate with a sinusoidal topography (**Figure 2**A, Movie S3, Supporting Information). Upon raising the pressure and nozzle height to ≈300 kPa and 2.25 mm, respectively, adjacent filaments form a contiguous layer on top of this wavy substrate (Figure 2B, Movie S3, Supporting Information). Solely to aid visualization, the printing parameters were selected to ensure that each filament remained distinct from one another. However, by modifying the volumetric flow rate of the inks at a constant printing speed (or vice versa), contiguous features can be printed. Finer filaments can also be printed by adding adapters that reduce their size of each nozzle, which yield thinner layers when interdigitated (Figure S4, Supporting Information). Due to the viscoelastic nature of this model ink, multiple layers can be printed in a layer-wise manner (Figure 2C,D, Movie S4, Supporting Information). Each of the 16 nozzles having the same velocity component in the print direction, variability in the substrate topography results in nonuniform nozzle tip speeds across the multinozzle array, which, in the absence of individual flow rate control, results in variations to cross-sectional areas of the deposited filaments. Similarly, the fixed spacing between each nozzle in the x-direction results in varying interfilament distance when deposited on a slanted surface. To quantify these deviations, filaments were deposited according to three base modes of operation: "pure roll" where the nozzle array progresses at an overall constant altitude while forming a roll angle φ with the horizontal plane, and two "pure pitch" modes (upwards and downwards), where the nozzles are horizontally aligned and move up, or down, along a flat plane forming a pitch angle θ with the underlying flat reference plane (Figure 2E). We observe that in all conditions (Figure 2F–H), the normalized cross-section area a and the interfilament distance d are in good agreement with theoretical predictions based upon geometrical and mass conservation considerations, as defined by:

$$a = \cos(\theta) \tag{1}$$

$$d = d_0/\cos(\varphi) \tag{2}$$

As expected, in a pure roll mode, the cross-sectional area of the printed ink filaments is independent of φ. The same is true for the interfilament spacing with respect to θ in a pure pitch mode. Given the high precision of the nozzle displacement in the z-direction (Figure S2, Supporting Information), the variations of the experimental values of interfilament spacing and cross-sectional areas to the theoretical predictions, can be primarily attributed to slight lateral play of the individual nozzles and minor differences in flow resistance within the tubing and manifold systems. For the roll, upward pitch, and downward pitch modes, respectively, the mean differences of the cross-sectional area values to the model were less than 5.2%, 7.7%, and 7.2%. Similarly, the mean differences of the interfilament spacing did not exceed 1%, 1.2% and 1.3%, respectively. Based on Equations (1 and 2), a roll angle of 17.75° and a pitch angle of 18.20° would result in a 5% variation in d and a, respectively. If a 10% variation is tolerable, φ and θ could reach up to 24.62° and 25.84°, respectively. Qualitatively, the roll printing mode introduces a slight skewing of the cross-section of the filament with

Figure 1. Multimaterial multinozzle adaptive 3D printing (MMA-3DP) platform. A) Schematic illustration of the 4-step workflow used for adaptive 3D printing. B) CAD representation of the adaptive multinozzle printhead system. C) CAD illustration of the nozzle actuation apparatus. D) Demonstration of multinozzle profile adaptation to three substrate models: flat (top), sinusoidal (middle), triangular (bottom). E) Rheological characterization of the model triblock copolymer ink. Left: Apparent viscosity as a function of shear rate. Right: Storage (G', solid circles) and loss (G'', open circles) moduli as a function of shear stress. F) Optical images of conformal printing of model triblock copolymer inks (dyed red and blue) on a complex substrate surface with a randomly generated topography. G,H) Optical image of the substrate after conformal printing of the single ink layer. (Scale bars: 10 mm).

© 2022 Wiley-VCH GmbH

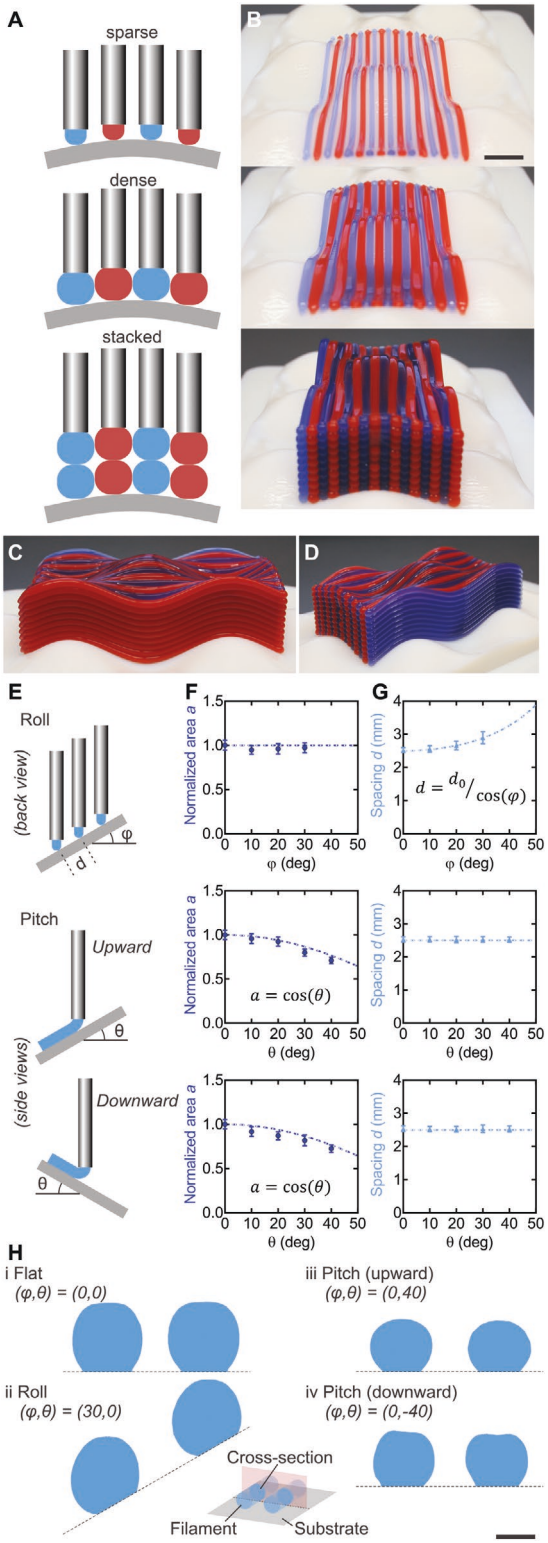

Figure 2. Different ink deposition and printing modes for multimaterial multinozzle adaptive 3D printing (MMA-3DP). A,B) Schematic illustration of ink deposition modes and corresponding optical images (edge view) of patterned features observed via adaptive 3D printing of triblock copolymer inks (dyed blue and red) on a substrate with a sinusoidally varying topography. C,D) Optical images (side views) of the 10-layer object shown in lower image in (B). E) Schematic illustrations of three printing modes used. F) Normalized cross-sectional area a of printed ink filaments as a function of the substrate incline angle. G) Interfilament distance d as a function of the substrate incline angle. H) Representative cross-sectional outlines (extracted from brightfield photographs) of filament pairs created using different print modes. (Scale bars: 10 mm in B and 1 mm in H).

the same magnitude as the roll angle φ itself (Figure 2Hii). The upward pitch mode leaves the filament shape relatively unaltered, although the diameter is reduced (Figure 2Hiii), while the downward pitch mode tends to result in the nozzle leaving a divot on the top surface of the filament for large values of θ (Figure 2Hiv). To correct for filament thinning at large values of pitch angle, future iterations of our MMA printheads will incorporate individual control over the volumetric flow rate of the inks. Moreover, both the nozzle actuation mechanism and ink supply systems will be miniaturized to improve pattern resolution.

To integrate stop/start capabilities, we incorporated two 8-way air manifolds with solenoid valves into our multinozzle printheads to control the pressurized air supply for each of the 16 individual ink containers (**Figure 3**A, Figure S5A, Supporting Information). The target voxelated design is inputted in the form of a binary image and discretized as an array of lines positioned 2.5 mm apart (or 1.25 mm in the interdigitated printing mode) (Figure 3B). In single nozzle DIW, a dwell at both the start and end of a printed filament is typically used to accommodate any delays in ink extrusion and to ensure proper contact with the substrate, respectively. However, in our MMA-3DP method, because each nozzle can extrude filaments independently of the other nozzles, any dwell in motion would result in material build up and therefore requires that the speed of the printhead remains constant. This constraint can lead to excess ink being dragged across the substrate when extrusion from a specific nozzle is halted and is exacerbated when the elastic energy stored in the ink or flexible tubing leads to excess ink oozing out of the nozzle. This phenomenon is responsible for the poor print quality shown in Figure 3C,D, which arises when printing in a "not corrected" (NC) mode. To improve print fidelity, the trajectory of each nozzle can be individually corrected, and the timing of ink deposition coordinated such that each nozzle hovers at a "safe" distance δh above the surface prior to translating downward as ink flow is initiated at a distance δd before printing a given filament (Figure 3C, "corrected" (C) mode). The values for δh and δd range between 3 and 5 mm, and 1 and 3 mm, respectively, depending on the ink rheology and printing parameters, i.e., nozzle size, printing speed and pressure used. We also implemented a slight dip in the nozzle height at the end of each printed filament before translating the nozzle upward to ensure proper filament termination. Together, these modifications to the nozzle trajectories result in higher pattern fidelity (Figure 3D, (C) mode). To demonstrate the ability to individually control (on/off) ink flow from each nozzle within the MMA printhead, a binary image of a crest symbol featuring the letter "H" was processed into three print paths of 16 filaments, resulting in a print area of 120×140 mm^2 (Figure 3E,F, Figure S5, Supporting Information). The symbol was printed using the model triblock copolymer

© 2022 Wiley-VCH GmbH

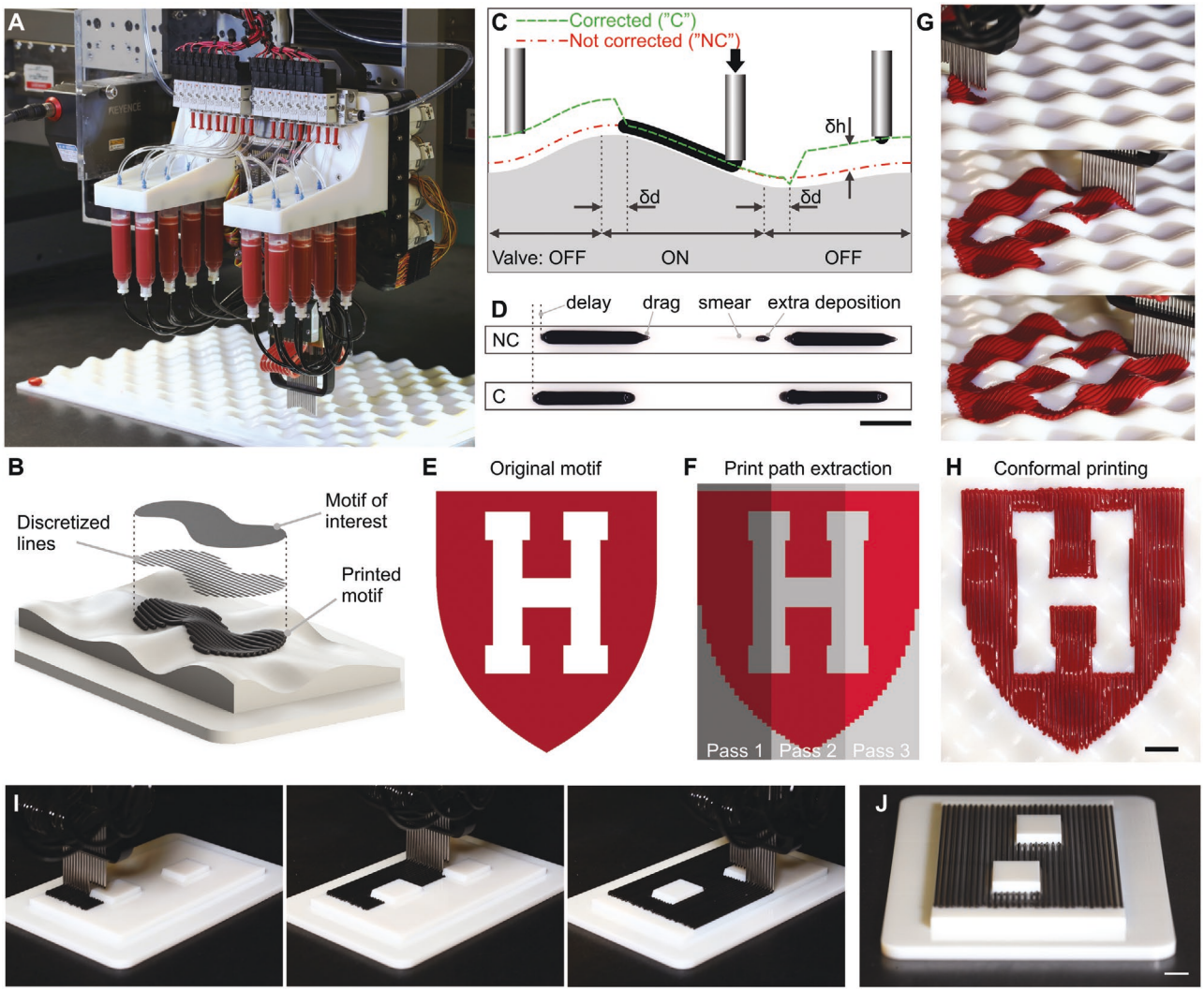

Figure 3. Multimaterial multinozzle adaptive 3D printing (MMA-3DP) with on/off ink flow. A) Experimental setup of the multinozzle printhead with an integrated array of 16 solenoid valves to control (on/off) ink dispensing on-the-fly. B) Illustration of the framework enabling the patterning of arbitrary motifs onto substrates with complex topographies. C) Schematic depicting the strategy employed for MMA-3DP to improve print quality and increase print fidelity. D) Comparison between print extrusions of Pluronic F-127 inks in the absence of trajectory correction (No correction or "NC", top) and with correction ("C", bottom). E) Crest motif serving as a model template to illustrate valve-enhanced MMA-3DP. F) Image discretization and print path extraction toward surface conformal patterning. G,H) Photographs showing the process of deposition of a Pluronic F-127 ink on the surface of a sinusoidal model substrate in the form of the motif of interest (shown in E). I,J) Photographs demonstrated the process of obstacle avoidance using valve-enable MMA-3DP. (Scale bars: 10 mm in D, 20 mm in H, and 10 mm in J).

ink described above (Figure 3G, Movie S5, Supporting Information), at a print speed of 2 mm s^{-1} and pressure of 386.1 kPa, resulting in its faithful representation on a sinusoidal substrate (Figure 3H). To illustrate the benefits of trajectory correction, we printed this same motif without correcting the nozzle print paths, which resulted in poor print fidelity (Figure S5B–E, Supporting Information). We then deposited a flat layer of this model ink onto a substrate that contains obstacles placed along the print path to show that our method is capable of faithfully depositing ink filaments even in the presence of irregularities on the substrate surface (Figure 3I,J, Movie S6, Supporting Information).

In two final demonstrations, we highlight the potential use of our MMA-3DP platform for wound and structural defect repair. In the first demonstration, we pattern an ink consisting of 4.5% porcine gelatin dissolved in phosphate buffer saline (**Figure 4**A). This ink exhibits similar apparent viscosity as the model triblock copolymer ink described above, but its plateau storage modulus of ≈0.22 kPa is considerably lower allowing each printed filament to merge with adjacent filaments thereby forming a cohesive layer (Figure 4B). To illustrate wound repair, a forearm model was abraded across a 135 × 33 mm^2 region on its top surface to simulate a large skin injury (Figure 4C). After generating the desired wound topography (Figure 4D), the gelatin ink is adaptively printed within the wound region (Figure 4E, Movie S7, Supporting Information), resulting in a conformal gelatin coating across the injured area (Figure 4F). Looking ahead, we plan

 © 2022 Wiley-VCH GmbH

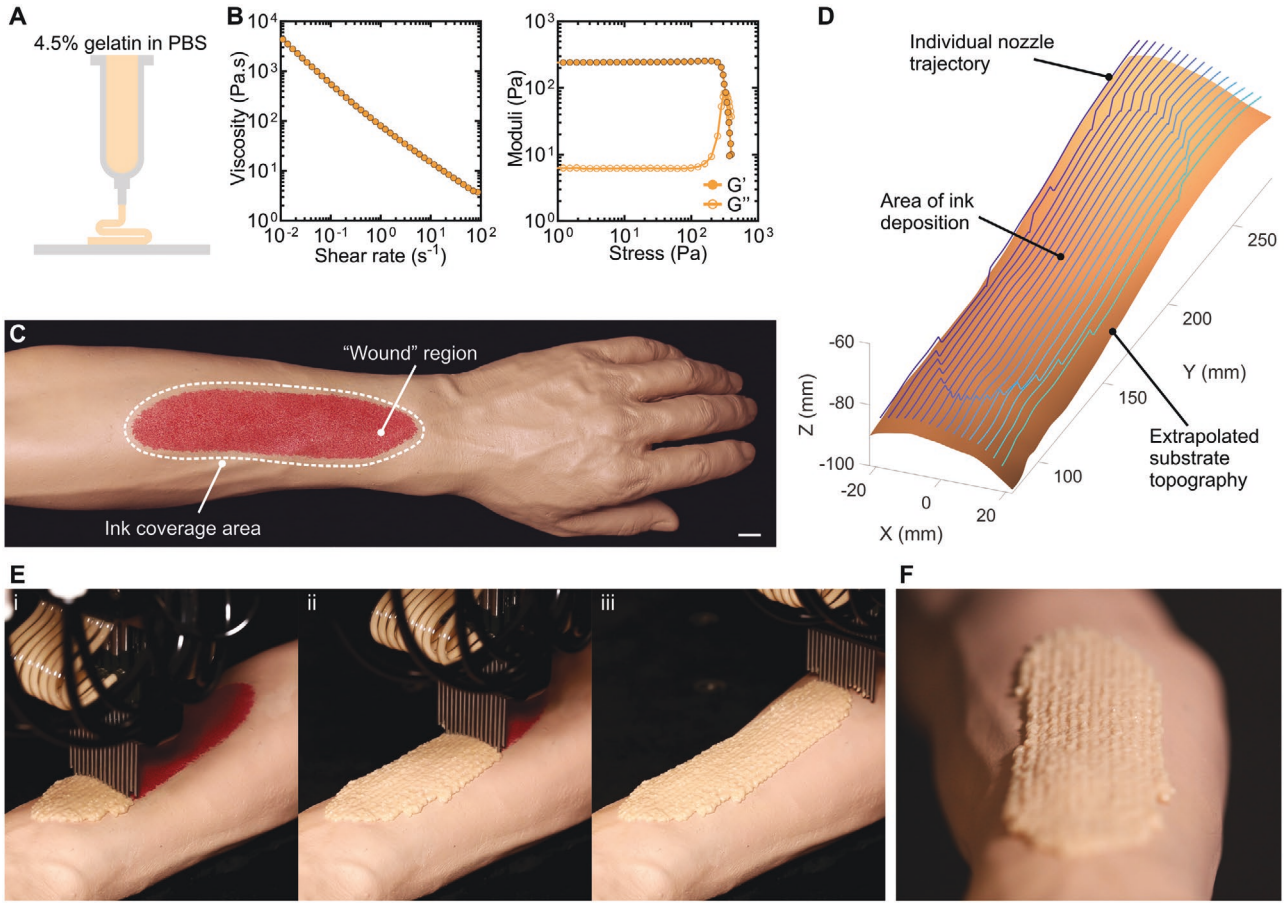

Figure 4. Multimaterial multinozzle adaptive 3D printing (MMA-3DP) of biological inks for wound healing. A) Biological ink composition. B) Flow curve (left) showing gelatin ink viscosity as a function of shear rate and amplitude sweep graph (right) showing storage (solid circles) and loss (open circles) moduli as a function of stress. C) Description of the forearm wound model to be covered with the gelatin ink by conformal printing. D) Representation of the model forearm topography with overlaid nozzle trajectories. E,F) Time lapse and final image of the biological ink patterned over the forearm model using MMA-3DP. (Scale bar: 10 mm).

to incorporate human dermal neonatal fibroblast cells within this ink to enable direct patterning of skin grafts[27,28], where the high throughput and adaptability of conformal printing platform would be quite beneficial.

The second demonstration focuses on defect filling of load-bearing, multimaterial architectures. Specifically, we used our MMA-3DP platform to restore the mechanical integrity of a 3D architecture composed of periodically arranged stiff and soft polyacrylate layers. Two structural inks were created: one ink (stiff ink), is composed of 1:1 ratio of urethane dimethacrylate (UDMA) and hydroxyethyl methacrylate (HEMA), while the other ink (soft ink) is composed of a 1:1 ratio of urethane acrylate oligomer (CN9021) and isodecyl acrylate (IDA) (**Figure 5**A). Their rheological properties are tailored by adding fumed silica, such that they exhibited the requisite viscoelastic behavior needed for filamentary printing (Figure 5B). Each ink exhibits nearly identical apparent viscosities as the model triblock copolymer ink over the same range of shear rates described above. These stiff and soft inks also have similar plateau storage moduli of 3 and 7 kPa and shear yield stress of 60 and 80 Pa, respectively. Upon printing, the inks are photopolymerized using blue light ($\lambda = 400$–500 nm) in an inert environment to prevent oxygen inhibition (Figure 5A), which leads to a dramatic difference in their respective Young's moduli of 73 MPa (stiff ink) and 0.9 MPa (soft ink) (Figure 5C–E). After printing the 3D multimaterial architecture ($50 \times 40 \times 22.5$ mm), a damaged region is introduced on its top surface via CNC milling (Figure 5F, Figure S6A,B, Movie S8, Supporting Information). Next, the defect is scanned and print paths are computed for each nozzle within the 16-nozzle array (Figure S6C,D, Supporting Information). MMA-3DP is then used to fill this large defect (Figure 5F,G, Movie S9, Supporting Information) thereby restoring its original shape and internal periodic arrangement of stiff and soft layers (Figure 5H,I). Finally, mechanical measurements are carried out to assess the Young's moduli of the original, damaged, and repaired periodic architectures, which correspond to 20.5 ± 3.1, 9.3 ± 1.3, and 14.5 ± 1.8 MPa ($n = 3$). The repaired 3D architectures exhibited a nearly identical stiff/soft periodicity as the original samples and their resulting deformation behavior under load (Movie S10, Supporting Information) indicates their stiffness is approximately 75% of the initial (undamaged) value (Figure 5J).

© 2022 Wiley-VCH GmbH

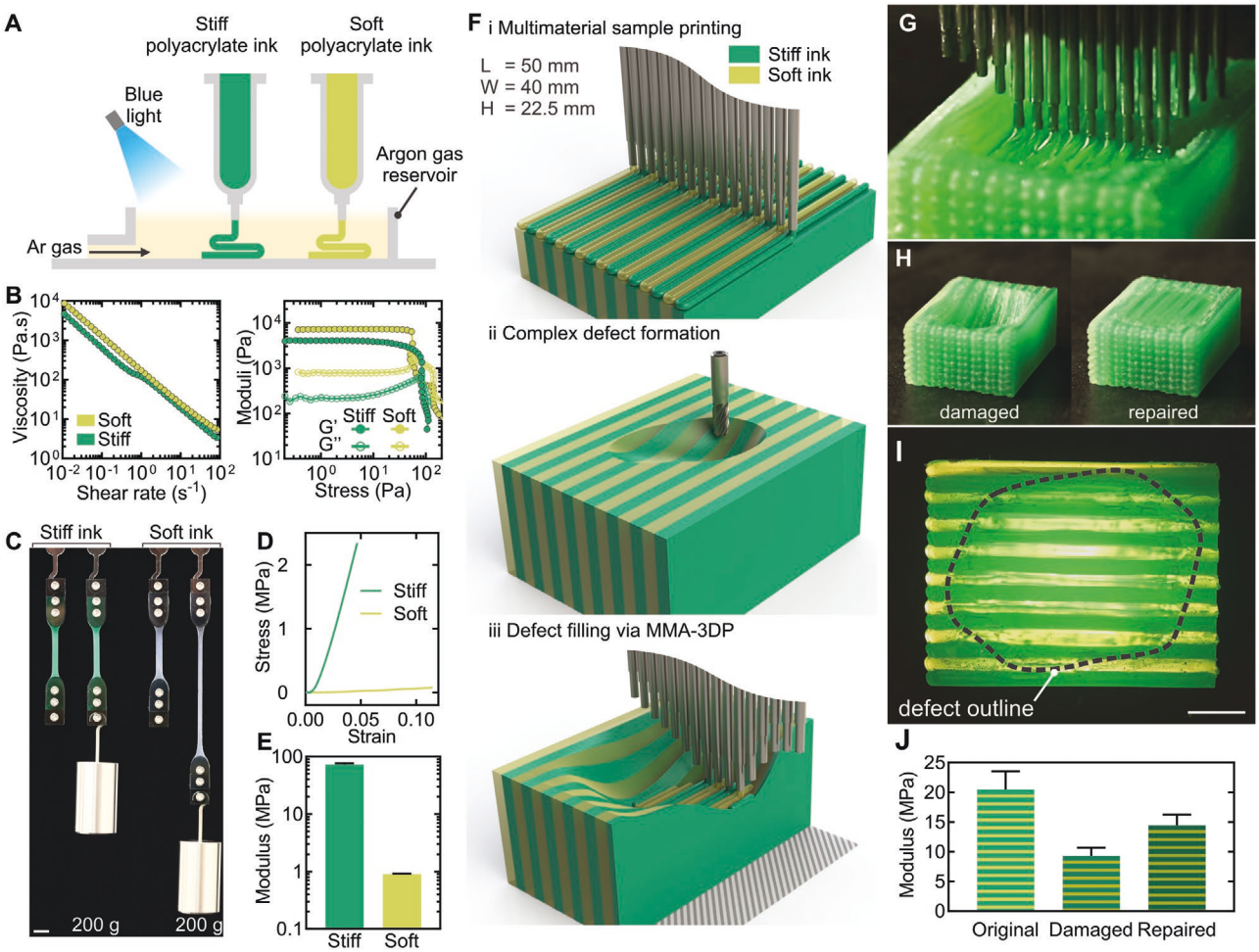

Figure 5. Multimaterial multinozzle adaptive 3D printing (MMA-3DP) of structural inks for damage repair. A) Structural ink compositions. B) Flow curves (left) showing the viscosity of the stiff and soft polyacrylate inks as a function of shear rate and amplitude sweep graph (right) showing storage (solid circles) and loss (open circles) moduli as a function of stress. C) Qualitative demonstration of the distinct mechanical properties of the stiff and soft ink materials. D) Representative compression stress–strain curves for both polyacrylate inks. E) Young's modulus values for both polyacrylates measured in the linear regime in stress–strain curves (as shown in (D). F) CAD representations of the framework used to demonstrate defect filling using MMA-3DP: multimaterial specimen printing with stiff-soft periodicity (i), complex defect formation by CNC machining (ii), and recovery of structural integrity by conformal printing (iii). G) Illustration of MMA-3DP of both polyacrylate inks into the defect cavity. H) Photographs comparing the damaged multimaterial specimen featuring the complex defect and the repaired specimen after defect filling by conformal printing. I) Image demonstrating the ability for the adaptive multinozzle to restore the periodic mechanical arrangement of the multimaterial specimen. J) Young's moduli of the original, damaged, and repaired multimaterial specimens. (Scale bars: 10 mm).

3. Conclusions

In summary, we have developed a multimaterial multinozzle adaptive 3D printing platform for rapidly patterning viscoelastic inks onto arbitrary 3D surfaces. Our platform opens new avenues for controlling the composition and architecture of soft materials in two- and three-dimensions. We have demonstrated the utility of this method by two exemplars focused on model skin wound and structural defect repair. In future embodiments, we envision incorporating nozzle designs that facilitate core-shell printing or active mixing to further enhance the complexity of these additively manufactured structures.

4. Experimental Section

Polymeric Inks: Several polymer-based inks were developed to demonstrate the utility of MMA-3DP. First, a model ink composed of an aqueous solution of 25 wt% triblock copolymer (Pluronic F127, BASF) was produced. First, the appropriate amount of Pluronic F127 was added to distilled water and cooled to 4 °C and shaken intermittently until the triblock polymer fully dissolves. This model ink was modified by adding either a red (Cadmium Red Medium) or blue (Cobalt Blue, Gamblin) pigment at a concentration of 0.2 w/w % or carbon black (Cancarb) at a concentration of 0.1 w/w % to yield red, blue, and black inks, respectively. Finally, a crimson ink was created by adding a pigment mixture of 15 parts white (Zink Oxide, Gamblin), 10 part red (Cadmium Red Medium, Gamblin), and 3 part blue (Cobalt Blue, Gamblin) at a total concentration of 1 w/w %. All model inks were loaded to the ink

© 2022 Wiley-VCH GmbH

reservoirs, which consisted of a 10 cc barrels (Nordson EFD), as a cold solution that undergoes gelation when warmed to room temperature prior to printing. If needed, the ink reservoirs were stored at room temperature to prevent pigment sedimentation.

Next, a biological ink was produced by first creating a 15 wt% stock solution of 300 Bloom type A porcine skin gelatin (Sigma-Aldrich) in phosphate buffer saline without calcium and magnesium (PBS-/-), heated at 90 °C for 8 h, sterile filtered, and neutralized with 5 N NaOH solution. This ink was further diluted by adding 4.5 wt% in PBS-/-. To match the color of the forearm model, a mixture of pigments composed of 200 parts white (Zink Oxide, Gamblin), 4 parts yellow (Cadmium Yellow Medium, Gamblin), 4 parts blue (Cobalt Blue, Gamblin), and 3 parts red (Cadmium Red Medium, Gamblin) were added to the final gelatin ink at a total concentration of 1 w/w%. The liquid gelatin ink was poured into the ink reservoirs, which consisted of a 10 cc barrels (Nordson EFD) and stored at 4 °C until printing.

Finally, two polyacrylate-based structural inks, denoted as stiff and soft inks, were produced. The stiff ink consisted of a mix of 50 wt% of a urethane dimethacrylate (UDMA) base (Sigma-Aldrich) and 49.5 wt% of hydroxyethyl methacrylate (HEMA, Sigma-Aldrich) as a thinner, while the soft ink consisted of 50 wt% of a commercially available urethane acrylate oligomer CN9021 base (Sartomer) and 49 wt% of isodecyl acrylate (IDA) thinner (Sigma-Aldrich). First, the base and thinner were mixed together using a centrifugal mixer (Speedmixer 600, FlackTek). Next, fumed silica (CAB-O-SIL TS-720 and CAB-O-SIL EH-5, Cabot) was added to the stiff and soft inks at concentrations of 6 and 8 wt%, respectively. The type of fumed silica and the ink formulation were optimized to yield similar rheological properties and therefore facilitate co-printing of both inks. The fumed silica was incorporated using the centrifugal mixer followed by three consecutive passes in a 3-roll mill. A photoinitiator phenylbisphosphine oxide (BAPO, Sigma-Aldrich) was added at concentration of 0.5 wt% (stiff ink) and 1 wt% (soft ink), prior to centrifugal mixing. For visualization purposes, the stiff ink was dyed with green food coloring at a concentration of 2 µL g^{-1}. The ink reservoirs (10 cc barrels or 6 fl oz cartridges) were back-filled from the outlets and centrifuged at 2000 rcf for 5 min to remove bubbles.

Ink Rheology: Rheological measurements were carried out on a stress-controlled rheometer (Discovery HR-3, TA Instrument). Measurements of the triblock copolymer and both polyacrylate inks were performed using a 40-mm plate with a corresponding upper cone geometry with a 2° angle. While measurements of the gelatin ink were performed using two 25-mm parallel plates, coated with sandpaper to prevent slip, at a gap distance of 1 mm. The gelatin ink was extruded onto the plate using a 1.36-mm dispensing tip (EFD Nordson) to emulate the printing process. Apparent viscosities of each ink were measured by flow sweeps carried out from shear rates of 0.01 to 100 s^{-1}. Oscillatory amplitude sweeps were carried out at a frequency of 0.5 Hz, from 1 to 400 Pa for the triblock copolymer ink, 0.01 to 300 Pa for the gelatin ink, and 0.2 to 200 Pa for the two polyacrylate inks. All measurements were carried out at room temperature.

Substrates with Complex Topography: All model substrates were 3D printed using Polyjet printers (Stratasys). The substrate with a sinusoidal topography was designed using the following surface equation for the height, z, expressed as a function of the plane coordinates x and y, resulting in a mogul field of amplitude 10 mm and period of 25 mm:

$$z(x,y) = 5 * \cos\left(\pi \frac{x}{25}\right) * \cos\left(\pi \frac{y}{25}\right) \tag{3}$$

resulting in a mogul field of amplitude 10 mm and period of 25 mm. The substrates with random topographies were constructed by fitting a 2D spline through a set of points, with x and y coordinated located along a 10 mm-spaced grid and with height values randomly generated within a 10 mm-range. The obstacle substrate consisted of a planar surface featuring two rectangles of dimension 20 mm in width and 26 mm in length and raised by 4 mm.

Topographic data was acquired using a line profilometer (Keyence LJ-V7300). This profilometer measures the height of 800 equally spaced (0.3 mm) points. The profilometer was mounted to one of the z-axes of the printer stage such that the scanning line was aligned with the x-direction (Figure S1A, Supporting Information). A map of the surface topography was generated by automatically advancing the profilometer in the y-direction by regular increments. For printhead alignment (see below), the step size was set to 0.3 mm. To determine the topography of the printing substrates, the step size was 1 mm. For surface areas larger than the width of the scanning line, multiple parallel passes were required. Data were collected using the LJ-Navigator 2 software (Keyence) and processed in a custom Matlab (MathWorks) routine. Raw data points were concatenated and smoothed in order to reconstruct the topography of the underlying substrate. The routine then extrapolated individual nozzle print paths from that data and generated camming tables featuring the heights of every one of the 16 nozzles, as well as the main multinozzle z-axis, as a function of the y-coordinates along the print path (Figure S2D, Supporting Information). To minimize the relative displacement and to maximize the absolute positioning range of each individual nozzle, the printhead (mounted on the 3-axis printer stage) follows a trajectory calculated as the midrange of all nozzle heights. (Figure S2D, Supporting Information). When coupled with the individual valving system (Figures 3 and 4), the print paths were altered to account for the additional nozzle displacements preceding and following ink dispensing along the regions of interest (Figure S5B,C, Supporting Information).

Adaptive Multimaterial Multinozzle Printheads: The individual components of the adaptive multinozzle system were mounted to a large frame machined out of acetal plastic (Figure 1B and Figure S1A, Supporting Information). The nozzle housing and the alignment bracket were machined out of brass and acetal plastic, respectively, and mounted onto the frame. Each nozzle tip was attached to two stainless steel rods (guiding and anti-rotation) sliding within a brass housing. The 40-mm-long anti-rotation rods and guiding rods were machined out of ground stainless steel stock (diameters 1/16″ and 3/16″, respectively, McMaster). The individual nozzle holders, along with the ink dispensing manifolds, were 3D printed on a high-resolution digital light processing (DLP) printer (Aureus, EnvisionTEC). A stainless steel 2-inch tube (ID 0.054″, OD 0.72″, McMaster), serving as the ink dispensing nozzle, together with the guiding and anti-rotation rods, were inserted into the 3D printed nozzle holder. One end of a flexible polyurethane tubing (ID 3/32″, OD 5/32″) was attached to the barbed inlet of the nozzle holder with the other end connected to the ink-dispensing manifold (Figure S1C, Supporting Information), which was itself fastened to the brass housing (Figure S1B, Supporting Information). The 16 sets of guiding rods were inserted into the same housing with a stainless steel compression spring (OD 0.187″, ID 0.147″, length 1.75″, rate 2.13 lbs/in, WB Jones) (Figure 1C). Each of the 16 nozzles was actuated by a 16 geared stepper motor (1/30.1 gear ratio, NMB Technologies) mounted to the back of the frame. Each stepper motor was equipped with a drive pulley, laser cut from acrylic sheets, and attached to the shaft of the motor (Figure 1B,C). Kevlar wires (0.014″ thread diameter, McMaster) were used to connect the end of the guiding rods to the drive pulleys, via custom-made pulleys mounted to the main frame.

The pulleys and wire were protected by a laser cut acrylic plate (Mini 18, Epilog), onto which was attached two 6 fl oz ink reservoirs (Figure S1C, Supporting Information) (Nordson EFD). Those reservoirs were supplied with compressed air via high-precision pressure controllers (Ultimus V, Nordson EFD), resulting in ink flow through tubing (ID 5/32″, OD 1/4″) connected to the 3D printed manifolds. The stepper motors were controlled by 16 drivers connected to a custom printed circuit board (PCB, OSH Park) (Figure S1D, Supporting Information). The PCB was attached to the front acrylic cover plate and connected to an A3200 motion controller equipped with four independent four-channel stepper motor controllers (NSTEP, Aerotech). Finally, the central frame was mounted to one of the z-axes of a motion control stage (Aerotech). In the valve-controlled version of the apparatus (Figure 3), the two 6 fl oz reservoirs were replaced by 16 10 cc cartridges (Nordson EFD), mounted to 2 custom-made and Polyjet-printed (Stratasys) racks, attached to the front cover on each side of the PCB (Figure 3A and Figure S5A, Supporting

© 2022 Wiley-VCH GmbH

Information). The pressurized air supplied to these barrels was controlled via 16 solenoid valves (SMC) mounted onto two manifolds (SMC).

Printhead Calibration: To determine the number of stepper motor increments per millimeter of nozzle displacement, a first theoretical estimate was calculated from the step angle of the stepper motors (0.212°), the radius of the drive pulleys (9.5 mm), and the microstep resolution of the stepper drivers (1/16), resulting in an approximate 455 inc mm^{-1}. This calibration was then refined by comparing the displacement readouts to the 10 mm height by which the nozzles were individually displaced using a gauge block. The average of three repeats was used as the final conversion coefficient. This step was repeated every 10 print sessions or when a part in the nozzle actuation chain was replaced.

MMA-3DP Platform: Prior to each print, the profilometer and the multinozzle frames were mounted on separate axes of the three-axis, motion-controlled stage and leveled (Figure S1A, Supporting Information). To zero each nozzle within the multinozzle array, the multinozzle frame was lowered such that the acetal alignment bracket was held at a distance of 35 mm from the granite stage surface. Every nozzle was then individually positioned 11 mm away from the counter using a gauge block (or 7 mm when using the 0.84-mm nozzle adapters) and zeroed at that location, resulting in the nozzle holders' starting position as the middle of their amplitude range.

Next, to determine the relative positions of the scanning profilometer with respect to the multinozzle printhead, an 18 mm-tall and 40-mm wide pyramid was used as a zeroing device. This device was 3D printed and mounted onto the printer stage (Figure S1E, Supporting Information). The leftmost and rightmost nozzles were then manually positioned above the tip of the pyramid to determine the position of the center of the printhead with respect to this reference. The pyramid was then scanned using the profilometer and a custom Matlab routine was used to extract the equation of 3 of the 4 pyramid side planes, the intersection of which provided the *x* and *y* coordinates of the tip of the pyramid and therefore linked its position to that of the profilometer. The difference of both reference positions resulted in the *x*- and *y*-offset values. To determine the *z*-offset between the printhead and the profilometer, the nozzles, zeroed within their housing, were brought in contact with the printer surface by lowering the three-axis stage and recording the axis height. The same surface was scanned to determine the height of the profilometer. The difference of both height values was used as the z-offset.

All ink reservoirs were allowed to reach room temperature before printing sessions. Regardless of the ink composition, each print session was preceded by a pressure calibration step. Straight lines along a flat substrate were generated at a nozzle height of interest, and extruding pressures were varied until the filaments reached the desired shape and diameter. This step was crucial for MMA-3DP of polyacrylate inks to ensure that the filament diameters matched between the stiff and soft inks. The substrates were scanned and their topographies extracted using the procedure described above. Finally, these inks were deposited, as a single or multiple layers, and using sparse, dense, and/or intercalated printing modes (Figure 2 and Figure S5, Supporting Information). The print speed, starting location, and distance of multinozzle displacement, as well as camming tables featuring the various height values for the 16 nozzles and the *z*-axis as a function of the *y*-coordinates were inputted into the GCode. When using the valving system, the print GCode also incorporated the *y*-coordinates and commands for ink starts and stops (on/off).

Ink Filament Characterization: Model ink filaments were printed on acrylic plates, mounted on two adjustable flip platforms (Thorlabs) to allow for the manually positioning at the various roll and pitch angles. To facilitate manipulation and imaging, the freshly printed filaments were cast in clear PDMS (Sylgard 184, Dow Corning). Once the PDMS was cured, the Pluronic ink was washed off and the imprints were filled with PDMS died with carbon black. The PDMS slabs were then sliced perpendicularly to the print direction into 2-mm thick sections and imaged using a stereomicroscope (Discovery.V20, Zeiss). Under Image J, the outlines of the filament cross sections were extracted and a custom Matlab routine was used to compute the inter-filament distance and normalize cross-section areas as a function of the roll and pitch angles.

Motion performance characterization: The line profilometer was installed below the MMA printhead with its beam facing upwards to measure the position of individual nozzles. To properly register the altitude of a nozzle, a small SLA-printed adapter was affixed to its tip. The raw data were processed in a custom Matlab routine.

3D Structural Architecture Printing and Milling: 3D architectures serving for the demonstration of the defect filling capabilities using MMA-3DP (Figure 5 and Figure S6, Supporting Information) were composed of periodic lamellae of stiff and soft polyurethane ink materials. Each architecture was printed using a fixed 16-nozzle array with similar spacing as the MMA printhead. The dispensing tips featured 0.84 mm-diameter adapter and 50-mm long filaments were deposited at a speed of 5 mm s^{-1} in the "intercalated" mode (Figure 5Fi, Figure S4A, Figure S6A, Movie S8, Supporting Information). Ink deposition was carried out in an inert environment to prevent oxygen inhibition by slowly injecting pressurized Argon gas in the bottom of an open acrylic container of dimensions 300 mm in width and 100 mm in height. The ink material was polymerized by supplying blue light (400–500 nm) from a distance of approximately 150 mm for 30 s using an Omnicure system (Excelitas Technologies) set to 100% intensity. Photopolymerization was carried out intermittently after every two layers (Figure S6A, Supporting Information) of a 20 layer structure was printed with overall sample dimensions 50× 40 × 22.5 mm. A modest reduction in sample height arises due to ink printing and photopolymerization. The complex defect topography was generated in Matlab. Based on that profile, a GCode routine was created and exported to a CNC machine. Using a 3mm ball-end mill, the defect was milled from the polyacrylate samples (Figure 5Fii, Figure S6B, Movie S8, Supporting Information).

The "damaged" samples were placed onto the printing platforms and aligned in *x*- and *y*-directions with the MMA-3D printheads. The profilometer was used to scan the surface of the defect and a custom Matlab routine extracted to the topography to generate the print paths and valving tables for each of the 16 nozzles (Figure S6C,D, Supporting Information). The defect filling procedure was carried out at a printing speed of 2.5 mm s^{-1}, using the same "intercalated" mode, 0.84-mm tip adapters, and Argon gas environment as for the building of the intact specimen (Figure 5Fiii,G, Movie S9, Supporting Information). Similarly, the photopolymerization of the inks was done every two layers with the same parameters as described above.

Mechanical Property Characterization: All mechanical tests were conducted on an electromechanical testing system (Instron 5566). The comparison between the mechanical properties of both stiff and soft polyacrylate materials was conducted on small disks (12 mm in diameter, 6 mm in thickness), cast and photopolymerized within acrylic molds. The compressive tests were carried out with a 1 kN load cell, at a rate of 0.003 mm s^{-1} over the course of 0.3 and 0.6 mm, for the stiff and soft ink materials, respectively. The Young's moduli were calculated in the linear region of the stress–strain curve using a custom Matlab script. For visualization purposes, tensile samples were created using acrylic molds with ISO 527 type 5A dimensions (75 mm overall length, 20 mm reduced section length, 4 mm width, 3 mm thickness). Samples were photographed at rest and under the load of a 200-g weight (Figure 5C). Before conducting the mechanical tests on the multimaterial lamellar printed samples, each multimaterial specimen of polyacrylate inks (50 × 40 × 22.5 mm) was faced using a CNC milling machine in order to render parallel the faces on which the load is applied. Mechanical tests were conducted using a 10 kN load cell. Samples were subject to cyclic compression tests with an amplitude of 2 mm, at a rate of 0.01 mm s^{-1}, over a total of five cycles. The data was processed in a custom Matlab routine and the Young's moduli were calculated at a strain of 3%.

Supporting Information

Supporting Information is available from the Wiley Online Library or from the author.

 © 2022 Wiley-VCH GmbH

Acknowledgements

The authors would like to thank James Weaver, Ted Sirota, Paul Machado and the Wyss machine shop, and Stan Cotreau and the SEAS machine shop for their assistance with hardware design and part fabrication, Mark Skylar-Scott and Jochen Mueller for their help with the valve control system, and Scott Slimmer and Daniele Foresti for insightful discussions. This research was primarily funded by the Office of Naval Research Vannevar Bush Faculty Fellowship program under award numbers N000141612823 and N00014-21-1-2958 as well as the National Science Foundation through both the Harvard MRSEC (DMR-2011754) and DMREF (DMR-1922321).

Conflict of Interest

J.A.L. is a member of the Scientific Advisory Boards of Autodesk, Azul3D, and Desktop Metal. J.A.L., S.G.M.U., and M.E. are inventors on a patent application related to this work filed by Harvard University (no. PCT/US2018/029132, filed on 24 April 2017). The authors declare that they have no other competing interests.

Author Contributions

S.G.M.U., R.D.W., M.E., and J.A.L. designed research; S.G.M.U., R.D.W, M.E., and D.K performed research; S.G.M.U., R.D.W, and M.E. analyzed data; and S.G.M.U., R.D.W., M.E., D.K and J.A.L wrote the manuscript.

Data Availability Statement

The data that support the findings of this study are available from the corresponding author upon reasonable request.

Keywords

3D printing, adaptive printheads, conformal, direct ink writing, soft materials

Received: January 22, 2022
Published online: March 13, 2022

[1] J. A. Lewis, *Adv. Funct. Mater.* **2006**, *16*, 2193.
[2] R. L. Truby, J. A. Lewis, *Nature* **2016**, *540*, 371.
[3] H. Yuk, B. Lu, S. Lin, K. Qu, J. Xu, J. Luo, X. Zhao, *Nat. Commun.* **2020**, *11*, 4.
[4] Y. L. Kong, I. A. Tamargo, H. Kim, B. N. Johnson, M. K. Gupta, T. W. Koh, H. A. Chin, D. A. Steingart, B. P. Rand, M. C. McAlpine, *Nano Lett.* **2014**, *14*, 7017.
[5] A. M. Golobic, M. D. Durban, S. E. Fisher, M. D. Grapes, J. M. Ortega, C. M. Spadaccini, E. B. Duoss, A. E. Gash, K. T. Sullivan, *Adv. Eng. Mater.* **2019**, *21*, 1900147.
[6] A. J. Blake, R. R. Kohlmeyer, J. O. Hardin, E. A. Carmona, B. Maruyama, J. D. Berrigan, H. Huang, M. F. Durstock, *Adv. Energy Mater.* **2017**, *7*, 1602920.
[7] B. G. Compton, J. A. Lewis, *Adv. Mater.* **2014**, *26*, 5930.
[8] C. Zhu, T. Y. J. Han, E. B. Duoss, A. M. Golobic, J. D. Kuntz, C. M. Spadaccini, M. A. Worsley, *Nat. Commun.* **2015**, *6*, 6962.
[9] C. Minas, D. Carnelli, E. Tervoort, A. R. Studart, *Adv. Mater.* **2016**, *28*, 9993.
[10] J. W. Boley, W. M. Van Rees, C. Lissandrello, M. N. Horenstein, R. L. Truby, A. Kotikian, J. A. Lewis, L. Mahadevan, *Proc. Natl. Acad. Sci. USA* **2019**, *116*, 20856.
[11] C. Xu, B. Quinn, L. L. Lebel, D. Therriault, G. L'espérance, *ACS Appl. Mater. Interfaces* **2019**, *11*, 8499.
[12] S. M. Sajadi, P. J. Boul, C. Thaemlitz, A. K. Meiyazhagan, A. B. Puthirath, C. S. Tiwary, M. M. Rahman, P. M. Ajayan, *Adv. Eng. Mater.* **2019**, *21*, 1801380.
[13] D. B. Kolesky, R. L. Truby, A. S. Gladman, T. a. Busbee, K. a. Homan, J. a. Lewis, *Adv. Mater.* **2014**, *26*, 3124.
[14] M. Kesti, C. Eberhardt, G. Pagliccia, D. Kenkel, D. Grande, A. Boss, M. Zenobi-Wong, *Adv. Funct. Mater.* **2015**, *25*, 7406.
[15] D. B. Kolesky, K. A. Homan, M. A. Skylar-Scott, J. A. Lewis, *Proc. Natl. Acad. Sci. USA* **2016**, *113*, 3179.
[16] Y. J. Choi, T. G. Kim, J. Jeong, H. G. Yi, J. W. Park, W. Hwang, D. W. Cho, *Adv. Healthcare Mater.* **2016**, *5*, 2636.
[17] X. Liu, H. Yuk, S. Lin, G. A. Parada, T. C. Tang, E. Tham, C. de la Fuente-Nunez, T. K. Lu, X. Zhao, *Adv. Mater.* **2018**, *30*, 1704821.
[18] N. Noor, A. Shapira, R. Edri, I. Gal, L. Wertheim, T. Dvir, *Adv. Sci.* **2019**, *6*, 1900344.
[19] L. Ouyang, J. P. K. Armstrong, Y. Lin, J. P. Wojciechowski, C. Lee-Reeves, D. Hachim, K. Zhou, J. A. Burdick, M. M. Stevens, *Sci. Adv.* **2020**, *6*, eabc5529.
[20] A. M. Duraj-thatte, A. Manjula-basavanna, J. Rutledge, J. Xia, S. Hassan, A. Sourlis, A. G. Rubio, A. Lesha, M. Zenkl, A. Kan, D. A. Weitz, Y. S. Zhang, N. S. Joshi, *Nat. Commun.* **2021**, *12*, 6600.
[21] Y. S. Zhang, G. Haghiashtiani, T. Hübscher, D. J. Kelly, J. M. Lee, M. Lutolf, M. C. McAlpine, W. Y. Yeong, M. Zenobi-Wong, J. Malda, *Nat. Rev. Methods Prim.* **2021**, *1*, 76.
[22] J. O. Hardin, T. J. Ober, A. D. Valentine, J. A. Lewis, *Adv. Mater.* **2015**, *27*, 3279.
[23] M. A. Skylar-Scott, J. Mueller, C. W. Visser, J. A. Lewis, *Nature* **2019**, *575*, 330.
[24] J. J. Adams, E. B. Duoss, T. F. Malkowski, M. J. Motala, B. Y. Ahn, R. G. Nuzzo, J. T. Bernhard, J. A. Lewis, *Adv. Mater.* **2011**, *23*, 1335.
[25] F. B. Coulter, B. S. Coulter, E. Papastavrou, A. Ianakiev, *3D Print. Addit. Manuf.* **2018**, *5*, 17.
[26] R. J. A. Allen, R. S. Trask, *Addit. Manuf.* **2015**, *8*, 78.
[27] R. Y. Cheng, G. Eylert, J. M. Gariepy, S. He, H. Ahmad, Y. Gao, S. Priore, N. Hakimi, M. G. Jeschke, A. Günther, *Biofabrication* **2020**, *12*, 025002.
[28] M. Albanna, K. W. Binder, S. V. Murphy, J. Kim, S. A. Qasem, W. Zhao, J. Tan, I. B. El-Amin, D. D. Dice, J. Marco, J. Green, T. Xu, A. Skardal, J. H. Holmes, J. D. Jackson, A. Atala, J. J. Yoo, *Sci. Rep.* **2019**, *9*, 1856.

 © 2022 Wiley-VCH GmbH